

Dissimilar welding of aluminum alloys 2024 T3 and 7075 T6 by TIG process with double tungsten electrodes

Liamine Kaba (✉ kaba05liamine@gmail.com)

CRTI: Centre de Recherche en Technologies Industrielles

Mohammed Elamine Djeghlal

Polytechnic National School (ENP)

Seddik Ouallam

Research Center in Industrial Technologies

Sami Kahla

Research Center in Industrial Technologies

Research Article

Keywords: 2024 and 7075 aluminum alloy, Aluminum with structural hardening, Microstructure, double electrode TIG Processing, dissimilar welding.

Posted Date: April 15th, 2021

DOI: <https://doi.org/10.21203/rs.3.rs-408163/v1>

License:  This work is licensed under a Creative Commons Attribution 4.0 International License.

[Read Full License](#)

Version of Record: A version of this preprint was published at The International Journal of Advanced Manufacturing Technology on September 10th, 2021. See the published version at <https://doi.org/10.1007/s00170-021-07888-5>.

Abstract

The aim of this work is to study the metallurgical and mechanical properties of dissimilar assemblies of 2024 T3 and 7075 T6 structural hardening aluminum alloy by TIG twine electrode arc welding process. It will include a weld performed according to optimized welding parameters followed by a study of the macroscopic and microscopic evolution of the dissimilar assembly (2024–7075) using optical and scanning electron microscopy (SEM); In addition, the phase compositions were analyzed with an energy dispersive spectrometer (EDS). Tensile and microhardness tests were performed. The tensile fracture was observed by SEM. We have found that this process thins the weld bead and reduces the size of the heat affected zone (HAZ) of the welded joint. The microhardness is lower in the melted area and higher on the side of the area affected by the heat especially for 7075 alloy, resulting in brittle strength and a sudden drop in breaking strength.

1. Introduction

Today, the search for new designs that allow either to fulfill a new functions or to lighten existing structures [1]. Aluminum and its alloys are some of the most widely used materials in the industry, especially in the aeronautics and aerospace industry.

The structural hardening alloys of the 7xxx and 2xxx series are the most widely used alloys; they are characterized by high mechanical strength and high corrosion resistance [2]. However, the assembly of these materials by welding is a challenge [3] for manufacturers and technologists, especially for heterogeneous assemblies. The difficulty stems from the high chemical reactivity of oxygen to aluminum, which produces a refractory layer of aluminum oxide and the high solubility of hydrogen, which generates porosities (blowholes). In addition, the high thermal conductivity generates lime cracks and deformations during welding ... etc. [4, 5, 6]. For this reason, research has been carried out to study the feasibility of heterogeneous joining of aluminum alloys using TIG, MIG, high energy LASER beam and lately FSW.

J. Y. Bai et al [7] found that TIG and MIG arc sources are more advantageous than high-energy beams due to their efficiency and economy. Laser-arc hybrid welding processes are considered as an efficient welding process; however, the deposition rate of the welding wire cannot be controlled independently of the welding current [8]. The FSW process allows several heterogeneous assemblies such as AA5754-AA7075 [9], AA2024-AA7075 [10], AA2219-AA5083 [11] and AA7075-AA6061 [12]. However, A.K. Lakshminarayanan et al [13] found that this process causes weakening at the bead (fusion zone) due to dissolution or growth of reinforcing precipitates during the thermal welding cycle.

The TIG welding process is an abbreviation for tungsten inert gas. Although it is a stable arc process with high quality weld beads, it suffers from low efficiency [14] where the deposition rate achieved is low compared to other welding processes. To overcome this shortcoming while retaining the benefits of TIG, a double electrode TIG welding technique has been developed [15].

Little research has been conducted on joining by ‘double electrode TIG’. It was initially launched by YAMADA et al. in 1998 [16]. Then, it was further developed by Kobayashi et al., who used two tungsten electrodes in a torch salt to improve the welding efficiency of thick plates of PCLNG (9% Ni-based steel) storage backs and obtained a higher deposit without sacrificing the advantages of the conventional TIG process [14]. Subsequently, Comparative studies conducted by WANG Bao [17] on low carbon steel sheets with thickness of 3 and 4 mm. revealed that welding by this process is significantly better than welding by the conventional process since it reduces welding defects such as metal collapse, pitting ... etc. Research is still ongoing, but in the theoretical view, there are simulations of the thermal phenomena of plasma arc welding.

In 2012, Guangjun Zhang & al [18] determined the dependence of temperature distribution of the coupling arc on the arc current, arc length and the distance between the two electrodes. He found that the maximum temperature in the high temperature region is located in the middle of the two electrodes while the maximum temperature of a single arc is located under the electrode. In 2014, Xinxin Wang et al [19] designed a numerical model that links the effect of plasma arc on the melt in the presence of oxygen in order to investigate the arc coupling behavior. The scope of the investigation included the distributions of temperature, velocity, pressure and current density, as well as the pattern of heat transfer and liquid flow in the melt exerted by the arc coupling. He found that the distributions of arc pressure, current density and heat flux at the anode are not rotationally symmetric, and cannot be described by Gaussian approximations. Another model was developed by Xueping Ding et al [20] to describe the arc characteristics of welding generated by the tungsten inert gas process with double electrode. He found that the simulated results indicate higher values of arc temperature obtained by helium gas compared to argon gas. Subsequently, in 2016 Schwedersky [21] presented two-dimensional measurements of pressure generated by the tungsten inert gas process with double electrode (T-TIG); he found that arc pressure values were much smaller for TIG with double electrode compared to those of TIG with a single electrode in the same total current. Moreover, he observed an electromagnetic interaction between the arcs, which varied according to the distance between the electrodes.

As revealed by the literature review, the studies on this technique have dealt with the welding of high-alloyed steels based on nickel (9 Ni) and steels with low carbon content, but have not taken into account metallurgical and mechanical aspects. For this reason, the aim of our work is to use this technique (TIG welding with double tungsten electrodes) for a metallurgical and mechanical study of a dissimilar weld of two aluminum alloys with structural hardening 2024–7075.

2. Materials And Methods

The experimental equipment includes two Miller Dynasty 350 TIG (AC/DC) current generators, three bottles of extra pure argon gas (99.9999%) to ensure the protection of the up and down molten bath, a cart to ensure the speed of the welding movement and a camera to capture the arc at the time of welding (Fig. 1).

For our system, to be a double electrode TIG process, the torches of the two generators are fixed in a jig on the carriage so that the electrodes are separated from each other and the height between the work pieces and the electrodes is ~ 4 mm.

The raw material of our base metals were sheets of aircraft-grade aluminum alloys of the type 2024 treated in the state T3 and type 7075 treated in the state T6 with a thickness of 2.5 mm. The assembly of the plates was carried out by filler wire of an aluminum alloy type ER: 5356 with 2 mm of diameter. The chemical and microstructural analyses of the latter were performed by a spark gap spectrometer and by metallography as shown in Table.1 and Fig. 2.

Before welding, the sheets were cut in to 200 x 100 mm pieces, then cleaned by a stainless steel wire brush to crush the oxide layer (Al_2O_3) and pickled by acetone to remove grease. Next, they were pointed butt to butt and fixed by a clamping system.

After welding, samples were cut, including transversal sections, polished with a series of abrasive papers from 220 to 4000, then the final polishing was done by a felt paper with a diamond suspension of grain of 3 and 1 μm . The sample was etched with a KELLER chemical solution (1 ml HF 48%, 1.5 ml HCl, 2.5 ml HNO_3 , 90 ml H_2O) for metallographic and SEM observations. The observations were made by an Nikon optical microscope (X1500 magnification), and a scanning electron microscope (SEM) brand ZEISS Gemini SEM 300 equipped with an energy dispersive spectrometer (EDS). To assess the quality of the mechanical properties of our welds, two tests were performed: the first was a microhardness test and the second was a tensile test. Microhardness measurements were determined with an automatic Vickers microhardness tester (BUEHLER WILSON VH3300). The tensile test was performed on a universal machine type MTS Criterion model 45, 100 KN; the test was applied to a specimen sized in Fig. 3.

3. Results And Discussions

To ensure the right choice of welding parameters, and to achieve a good arc stability, several studies were conducted on the current intensity, the voltage and the shielding gas flow; Table 2 presents our choices of the welding parameters with a double electrode TIG .

The visual inspection of the bead shows a neat aspect on both the up and down sides without any defects (cracks or channels, etc.) all along the welding joints, which can be explained by the good superposition of the solidification stripes on each other. The average width is about 8 mm on the upside and 6 mm on the down side. The mechanical strength of the welds is often related to the structural morphology and the presence of secondary phase particles in the matrix. The chemical nature, quantity and location of these particles will be important parameters for understanding the phenomena related to the lowering of mechanical properties that generate sharp rupture [23].

3.1. Microhardness

Figure 6 shows the evolution of the microhardness profiles measured across the welded joint from left to right, including the base metals (MB 2024 to MB 7075), the heat-affected zones (ZAT 2024, ZAT 7075), the liaison zones (ZL 2024, ZL 7075), and the fusion zone (ZF), as shown in Fig. 6. Vickers indenter is applied on the cross section under a load of 300 g with a pitch of 300 μm .

It can be seen that the microhardness is more basic in the molten zone with an average value of 96 HV, followed by an increase to about 109 HV and 125 HV in the bonding zones ZL2024, and ZL7075 successively; then a rapid increase up to a maximum value of 148 Hv and 185 HV in the heat affected zones of ZAT2024 and ZAT7075 respectively. This increase is followed by a drop in microhardness in both metals especially the base metal side 2024 decreasing down to 107 HV approximately. Finally, a return of increase with an average value of 125 HV in our base metal MB2024 and MB7075 is observed.

3.2. Macrostructures and Microstructures Analysis

The metallographic observations were made on the plane perpendicular to the rolling direction. Figure 7 presents the macrography of the weld bead, where we can distinguish several zones such as the molten zone (ZF), liaison zone (ZL), thermally affected zone (ZAT), and finally the base metal (MB).

These changes in microstructure related to temperature gradients have been addressed in many different works [24]. However, the literature is poor in studies of heterogeneous weld joints of aluminum alloys as is the case of double electrode TIG welding processes.

As shown in Fig. 7, the molten zone (MZ) is of the order of $\approx 8 \text{ mm}$, the bonding zones of $\approx 0.6 \text{ mm}$ and finally the thermally affected zones (HAZ) of the order of $\approx 4 \text{ mm}$.

Figure 2 above shows the metallographic structure of the base metals. It can be seen that the structure of both metals are elongated grains, which can be attributed to the lamination effect, with dark coarse precipitates.

The main coarse particles are impurity phases or equilibrium phases. In general, the insoluble particles are the coarsest with irregular forms and complex compounds of the chemical elements Fe, Cu, Si and Al [25]. On the other hand, the equilibrium phases are the fine particles with round forms [26, 27]. Figure 8 shows SEM micrographs and maps of the distribution of the chemical elements of the base metals.

We can see that the irregular particles are rich in Fe and Cu, proving the presence of the $\text{Al}_7\text{Cu}_2\text{Fe}$ phase, and the observed round particles can be identified as equilibrium precipitates θ (Al_2Cu), S (Al_2CuMg) Fig. 8.a; thus, the η (Mg_2Zn) phase Fig. 8.b.

Figure 9. shows the central zone of the weld (molten zone ZF). This zone is obtained from a liquid/solid transformation; with a rather slow solidification [28]. A marked segregation is also apparent in this zone. In terms of grain structure, it is characterized by a dendritic equiaxed structure [26] with an aluminum solid solution ($\alpha\text{-Al}$) contoured by grain boundaries.

From the chemical element mappings (Fig. 9), it can be seen that the interdendritic grain boundary particles were identified with a copper (Cu) rich, zinc (Zn) weak magnesium (Mg) phase to form the ternary phase S ($\text{Al}_2\text{Cu}-\text{Mg}$), explained by F.Lefebre and C.G.Rhodes as an eutectic of type $\alpha\text{-Al} + \theta(\text{Al}_2\text{Cu})$ and $\text{Al}-\text{Zn}-\text{Mg}$ [28, 30].

At the end of the molten zone, partially molten bonding zones are formed as shown in Fig. 10; they are heated above the solidus and eutectic temperature. They are characterized by elongated columnar grains with some epitaxy developing in the opposite direction to the heat removal [31].

From the EDS chemical analysis maps, we find that liquefactions are formed at the boundaries of the grain boundaries, which contain intermetallic phases of the type Al_2Cu [32], Al_2CuMg plus eutectic $\text{Al}-\text{Cu}-\text{Mg}$ [33] in the 2024 side, MgZn_2 , $\text{Mg}(\text{Al}, \text{Zn})_2$ plus eutectic $\text{Al}-\text{Zn}-\text{Mg}$ [30] on the 7075 side. When our alloys are heated rapidly above the solvus temperature, the intermetallics and residual eutectic do not have enough time to dissolve completely in the matrix because solid state diffusion is slow. Therefore, when heated to the eutectic temperature, the residual intermetallic phase reacts with the matrix and forms the liquid eutectic at the interface [31].

Just next to the partially melted zones, heat affected zones are presented in Fig. 11. During solidification, the temperature is below solidus, therefore, it is too low for the formation of a melt, but sufficient to provoke important microstructural modifications. These areas are undergoing solid/solid transformations, and precipitation and grain growth are observed [34].

As shown in the MAB micrographs and the EDS chemical analysis maps, we find that there is a magnification in the vicinity of the partially melted zones on both sides (2024 and 7075.A.F). Norman [35] and A. Elrefaey [36] have well explained the sequence of precipitates in the structural aluminum alloys talc 2024 and 7075 and confirmed by transmission electron microscopy (TEM) that in the vicinity of the solvus temperature an absence of the $\text{Al}-\text{Cu}-\text{Mg}$ and $\text{Al}-\text{Zn}-\text{Mg}$ phases, which causes a natural aging to occur thereafter, restoring the properties of the base alloy, which also increases the microhardness.

At some distance from the partially melted zones (center of the HAZ), the temperature is below the solvent temperature and above 200°C; the predominant phases are S in alloy 2024 [35] and η in alloy 7075 [36]. This will induce overaging, where any precipitate will be coarse and will inevitably produce an aged microstructure with a decrease in microhardness.

Finally, the HAZ areas are adjacent to the base metals where the temperature is below 200°C; the base materials (2024 and 7075) recover an artificial aging treatment and will produce precipitations of the reinforcing phase S' and η' (Mg Zn_2) of the base metals respectively, which increases the microhardness [37].

3.3. Traction

In general, the tensile test is a destructive test used for the purpose of characterizing the mechanical behavior and evaluating the mechanical properties of traction such as: yield strength, maximum tensile

strength, elongation [38]. For this purpose, the test was carried out on a universal machine, with a tensile speed of 0.05 mm/s; the specimens were taken perpendicular to the direction of welding.

Figure 12 shows the micrograph of the fracture surfaces of the dissimilar assembly tensile specimen (2024–7075) while the results of the tensile test are presented in Table 3.

Table 3. Mechanical properties of tensile tests

As shown in the table, the maximum tensile strengths of 7075T6 and 2024 T3 base metals are 515.89 and 459.67 MPa, respectively. Thus, the elongation and maximum tensile strength of the welded joint are 2.62% and 288.35 MPa, respectively. This shows a 44% and 37% reduction in the strength of the welded joint unlike those of the base metals 7075 and 2024, respectively. However, the results obtained from this work are satisfactory because they are consistent with works involving friction stir welding technique such as those done by V. Saravanan et al [39], R. Padmanaban [40] and Avinash P [41].

One can see that the weld is fractured at the bond area on the 7075 T6 alloy side (Fig. 12. Band c).

SEM micrographs of the fracture surfaces (Fig. 12d and e) show that the fracture surface is intergranular. As shown in the microstructures and microhardness profiles, this area contains brittle precipitates with a significant microhardness. In addition, the faces seem to be brittle failures since the surfaces are flat and show almost no signs of plastic deformation [42].

4. Conclusion

In this work, sheets of dissimilar aluminum alloys (2024 and 7075) were welded by TIG arc welding process with double tungsten electrodes and the microstructural and mechanical properties of joint are studied. The main findings are summarized as follows:

1. The stable arc with double tungsten electrodes preceding TIG will produce good weld bead aspects explained by the good superposition of solidification striations, and the lack of microscopic defects such as porosities. This has a positive effect on the quality of the weld.
2. The energy dissipated by the heat source creates several zones (molten zone, heat affected zones), which can be explained by structural changes.
3. The heat affected zones are reduced compared to the conventional TIG welding process. Precipitates of the type Al_2Cu (θ phase) and $\text{Al}_2\text{Cu Mg}$ (S phase) and η (MgZn_2) are formed in the heat affected zone.
4. The hardness is lower in the molten zone because the hardening precipitates are dissolved during melting and no structural hardening reaction takes place at this temperature.
5. The maximum load of the 2024 T3-7075 T6 assembly is satisfactory since it can converge to the maximum load with the friction stir welding technique. Despite the brittle fracture.

Declarations

Acknowledgments The authors wish to express their sincere appreciations to the Research Center in Industrial Technologies (CRTI) and Special thanks to the Laboratory of Science and Materials Engineering (LSGM).

Funding

This research received no specific grant from any funding agency in the public, commercial, or not-for-profit sectors.

Ethics approval

Not applicable.

Consent to participate

Not applicable.

Consent to publish

The authors give all the rights to publish the material presented in this work.

Authors Contributions

All authors contributed to the research, writing, and reviewing of the paper.

Competing interests

The authors declare no competing interests.

Availability of data and materials

All the data have been presented in the manuscript.

References

1. Toma, C. M. (2012). Maîtrise des interfaces hétérogènes lors d'une opération de soudo-brasage: application au couple aluminium-magnésium (Doctoral dissertation, Dijon).
2. Troeger, L. P., & Starke Jr, E. A. (2000). Microstructural and mechanical characterization of a superplastic 6xxx aluminum alloy. *Materials Science and Engineering: A*, 277(1-2), 102-113. [https://doi.org/10.1016/S0921-5093\(99\)00543-2](https://doi.org/10.1016/S0921-5093(99)00543-2)
3. Al-Roubaiy, A. O., Nabat, S. M., & Batako, A. D. (2014). Experimental and theoretical analysis of friction stir welding of Al–Cu joints. *The International Journal of Advanced Manufacturing Technology*, 71(9), 1631-1642. <https://doi.org/10.1007/s00170-013-5563-z>

4. Sheikhi, M., Ghaini, F. M., & Assadi, H. (2015). Prediction of solidification cracking in pulsed laser welding of 2024 aluminum alloy. *Acta Materialia*, 82, 491-502.
<https://doi.org/10.1016/j.actamat.2014.09.002>
5. Caiazzo, F., Alfieri, V., Cardaropoli, F., & Sergi, V. (2013). Butt autogenous laser welding of AA 2024 aluminium alloy thin sheets with a Yb: YAG disk laser. *The International Journal of Advanced Manufacturing Technology*, 67(9), 2157-2169. <https://doi.org/10.1007/s00170-012-4637-7>
6. Cho, J., Lee, J. J., & Bae, S. H. (2015). Heat input analysis of variable polarity arc welding of aluminum. *The International Journal of Advanced Manufacturing Technology*, 81(5), 1273-1280. <https://doi.org/10.1007/s00170-015-7292-y>
7. Bai, J. Y., Fan, C. L., Yang, C. L., & Dong, B. L. (2016). Effects of thermal cycles on microstructure evolution of 2219-Al during GTA-additive manufacturing. *The International Journal of Advanced Manufacturing Technology*, 87(9), 2615-2623. <https://doi.org/10.1007/s00170-016-8633-1>
8. Wang, J. B., Nishimura, H., Katayama, S., & Mizutani, M. (2013). Welding of aluminium alloy by using filler-added laser-arc hybrid welding process. *Welding International*, 27(2), 98-108.
<https://doi.org/10.1080/09507116.2011.600013>
9. Kasman, S., & Yenier, Z. (2014). Analyzing dissimilar friction stir welding of AA5754/AA7075. *The International Journal of Advanced Manufacturing Technology*, 70(1-4), 145-156.
<https://doi.org/10.1007/s00170-013-5256-7>
10. Song, Y., Yang, X., Cui, L., Hou, X., Shen, Z., & Xu, Y. (2014). Defect features and mechanical properties of friction stir lap welded dissimilar AA2024-AA7075 aluminum alloy sheets. *Materials & Design*, 55, 9-18. <https://doi.org/10.1016/j.matdes.2013.09.062>
11. Mastanaiah, P., Sharma, A., & Reddy, G. M. (2016). Dissimilar friction stir welds in AA2219-AA5083 aluminium alloys: effect of process parameters on material inter-mixing, defect formation, and mechanical properties. *Transactions of the Indian Institute of Metals*, 69(7), 1397-1415.
<https://doi.org/10.1007/s12666-015-0694-6>
12. Hasan, M. M., Ishak, M., & Rejab, M. R. M. (2017). Influence of machine variables and tool profile on the tensile strength of dissimilar AA7075-AA6061 friction stir welds. *The International Journal of Advanced Manufacturing Technology*, 90(9-12), 2605-2615. <https://doi.org/10.1007/s00170-016-9583-3>
13. Lakshminarayanan, A. K., Balasubramanian, V., & Elangovan, K. (2009). Effect of welding processes on tensile properties of AA6061 aluminium alloy joints. *The International Journal of Advanced Manufacturing Technology*, 40(3-4), 286-296. <https://doi.org/10.1007/s00170-007-1325-0>
14. Kobayashi, K., Nishimura, Y., Iijima, T., Ushio, M., Tanaka, M., Shimamura, J., ... & Yamashita, M. (2004). Practical application of high efficiency twin-arc TIG welding method (SEDAR-TIG) for PCLNG storage tank. *Welding in the World*, 48(7), 35-39 . <https://doi.org/10.1007/BF03266441>
15. Zhang, G., Xiong, J., Gao, H., & Wu, L. (2012). Effect of process parameters on temperature distribution in twin-electrode TIG coupling arc. *Journal of Quantitative Spectroscopy and Radiative Transfer*, 113(15), 1938-1945. <https://doi.org/10.1016/j.jqsrt.2012.05.018>

16. Kobayashi, K., YUKI, M., TEJIMA, A., & NISHIMURA, Y. (2002). Development of high efficiency TIG welding method (SEDAR-TIG). *Ishikawajima-Harima Giho*, 42(3), 127-132. <http://pascal-francis.inist.fr/vibad/index.php?action=getRecordDetail&idt=13700607>
17. Wang, S., ZHANG, H., LENG, X., & WU, L. (2007). Twin-electrode TIG welding procedure and mechanism of weld formation. *TRANSACTIONS-CHINA WELDING INSTITUTION*, 28(2), 21.
18. Zhang, G., Xiong, J., Gao, H., & Wu, L. (2012). Effect of process parameters on temperature distribution in twin-electrode TIG coupling arc. *Journal of Quantitative Spectroscopy and Radiative Transfer*, 113(15), 1938-1945. <https://doi.org/10.1016/j.jqsrt.2012.05.018>
19. Wang, X., Fan, D., Huang, J., & Huang, Y. (2014). A unified model of coupled arc plasma and weld pool for double electrodes TIG welding. *Journal of Physics D: Applied Physics*, 47(27), 275202. <https://doi.org/10.1088/0022-3727/47/27/275202>
20. Ding, X., Li, H., Yang, L., Gao, Y., & Wei, H. (2014). Numerical analysis of arc characteristics in two-electrode GTAW. *The International Journal of Advanced Manufacturing Technology*, 70(9-12), 1867-1874. <https://doi.org/10.1007/s00170-013-5443-6>
21. Schwedersky, M. B., Gonçalves e Silva, R. H., Dutra, J. C., Reisgen, U., & Willms, K. (2016). Two-dimensional arc stagnation pressure measurements for the double-electrode GTAW process. *Science and Technology of Welding and Joining*, 21(4), 275-280. <https://doi.org/10.1080/13621718.2015.1104095>
22. Ogino, Y., Hirata, Y., & Nomura, K. (2011). Numerical analysis of the heat source characteristics of a two-electrode TIG arc. *Journal of Physics D: Applied Physics*, 44(21), 215202. <https://doi.org/10.1088/0022-3727/44/21/215202>
23. Puydt, Q. (2012). Comportement mécanique de soudures en alliage d'aluminium de la série 7xxx: de la microstructure à la modélisation de la rupture (Doctoral dissertation, Institut National Polytechnique de Grenoble-INPG).
24. Bousquet, E. (2011). Durabilité des assemblages soudés par friction stir Welding (FSW) Corrélation entre microstructure et sensibilité à la corrosion (Doctoral dissertation, Ph. D. thesis, Université Bordeaux 1).
25. Lin, Y. C., Xia, Y. C., Jiang, Y. Q., Zhou, H. M., & Li, L. T. (2013). Precipitation hardening of 2024-T3 aluminum alloy during creep aging. *Materials Science and Engineering: A*, 565, 420-429. <https://doi.org/10.1016/j.msea.2012.12.058>
26. Cochard, A., Zhu, K., Joulié, S., Douin, J., Huez, J., Robbiola, L., ... & Brunet, M. (2017). Natural aging on Al-Cu-Mg structural hardening alloys—Investigation of two historical duralumins for aeronautics. *Materials Science and Engineering: A*, 690, 259-269. <https://doi.org/10.1016/j.msea.2017.03.003>
27. Kaçar, H., Atik, E., & Meriç, C. (2003). The effect of precipitation-hardening conditions on wear behaviours at 2024 aluminium wrought alloy. *Journal of Materials Processing Technology*, 142(3), 762-766. [https://doi.org/10.1016/S0924-0136\(03\)00642-3](https://doi.org/10.1016/S0924-0136(03)00642-3)

28. Lefebvre, F., Ganguly, S., & Sinclair, I. (2005). Micromechanical aspects of fatigue in a MIG welded aluminium airframe alloy: Part 1. Microstructural characterization. *Materials Science and Engineering: A*, 397(1-2), 338-345. <https://doi.org/10.1016/j.msea.2005.02.051>
29. Liang, Y., Shen, J., Hu, S., Wang, H., & Pang, J. (2018). Effect of TIG current on microstructural and mechanical properties of 6061-T6 aluminium alloy joints by TIG–CMT hybrid welding. *Journal of Materials Processing Technology*, 255, 161-174. <https://doi.org/10.1016/j.jmatprotec.2017.12.006>
30. Rhodes, C. G., Mahoney, M. W., Bingel, W. H., Spurling, R. A., & Bampton, C. C. (1997). Effects of friction stir welding on microstructure of 7075 aluminum. *Scripta materialia*, 36(1), 69-75.
31. Kaufman, J. G. (2000). Introduction to aluminum alloys and tempers. ASM international.
32. Alfieria, V., Caiazzo, F., & Sergi, V. (2015). Autogenous laser welding of AA 2024 aluminium alloy: process issues and bead features. *Procedia Cirp*, 33, 406-411.
<https://doi.org/10.1016/j.procir.2015.06.094>
33. Rosalie, J. M., & Bourgeois, L. (2012). Silver segregation to θ' (Al₂Cu)–Al interfaces in Al–Cu–Ag alloys. *Acta Materialia*, 60(17), 6033-6041. <https://doi.org/10.1016/j.actamat.2012.07.039>
34. Kou, S. (2003). Welding metallurgy second edition. Hoboken, New Jersey, 1-29.
35. Norman, A. F., Drazhner, V., & Prangnell, P. B. (1999). Effect of welding parameters on the solidification microstructure of autogenous TIG welds in an Al–Cu–Mg–Mn alloy. *Materials Science and Engineering: A*, 259(1), 53-64. [https://doi.org/10.1016/S0921-5093\(98\)00873-9](https://doi.org/10.1016/S0921-5093(98)00873-9)
36. Elrefaey, A. (2015). Effectiveness of cold metal transfer process for welding 7075 aluminium alloys. *Science and Technology of Welding and Joining*, 20(4), 280-285.
<https://doi.org/10.1179/1362171815Y.00000000017>
37. Kalita, S. J. (2011). Microstructure and corrosion properties of diode laser melted friction stir weld of aluminum alloy 2024 T351. *Applied Surface Science*, 257(9), 3985-3997.
<https://doi.org/10.1016/j.apsusc.2010.11.163>
38. Jalilvand, V., Omidvar, H., & Khorrami, H. (2014). Effect of welding parameters on the mechanical properties of AA2024 aluminium alloy joints welded by resistance seam welding. *Canadian Metallurgical Quarterly*, 53(2), 117-124. <https://doi.org/10.1179/1879139513Y.0000000110>
39. Saravanan, V., Rajakumar, S., Banerjee, N., & Amuthakkannan, R. (2016). Effect of shoulder diameter to pin diameter ratio on microstructure and mechanical properties of dissimilar friction stir welded AA2024-T6 and AA7075-T6 aluminum alloy joints. *The International Journal of Advanced Manufacturing Technology*, 87(9), 3637-3645. <https://doi.org/10.1007/s00170-016-8695-0>
40. Padmanaban, R., Balusamy, V., & Vaira Vignesh, R. (2020). Effect of friction stir welding process parameters on the tensile strength of dissimilar aluminum alloy AA2024-T3 and AA7075-T6 joints. *Materialwissenschaft und Werkstofftechnik*, 51(1), 17-27.
<https://doi.org/10.1002/mawe.201800184>
41. Avinash, P., Manikandan, M., Arivazhagan, N., Ramkumar, K. D., & Narayanan, S. (2014). Friction stir welded butt joints of AA2024 T3 and AA7075 T6 aluminum alloys. *Procedia Engineering*, 75, 98-102.
<https://doi.org/10.1016/j.proeng.2013.11.020>

42. Menan, F. (2008). Influence de la corrosion saline sur la tolérance aux dommages d'un alliage d'aluminium aéronautique 2XXX (Doctoral dissertation, Poitiers)

Tables

Table 1 Chemical composition of base metal and filler metals (wt.%).

Element		Al	Si	Fe	Cu	Mn	Mg	Zn	Ti	Cr
Bases metals	2024 T3	93.5	0.087	0.20	> 4	0.55	1.36	0.1	0.011	0.007
	7075 T3	87.85	0.54	0.30	1.74	0.25	3.08	5.33	0.26	0.2
Filler metal	ER : 5356	93.7	0.25	0.40	0.10	12.5	5.2	0.10	0.11	0.11

Table 2 Welding parameters.

Welding process	N° Welding pass	Wire diameter (mm)	Welding current I (A)	Welding voltage U (V)	Welding speed v (mm/s)	Flow rate Q (l/min)	Welding energy E (j/mm)
TIG	1 st pass (up)	2	60-60	9.5-9.5	3	15	266
TIG	2 nd pass (dawn)	2	60-60	9.5-9.5	3	15	226

Table 3. Mechanical properties of tensile tests

Material	Ultimate tensile strength (MPa)	Yield strength 0.2% (MPa)	Elongation (%)
Bases metals 2024 T3	459,67	288,56	12,23
Bases metals 7075 T6	515,89	460,054	7,54
Welding metals	288,35	120,72	2,62
2024 T3-7075 T6			

Figures

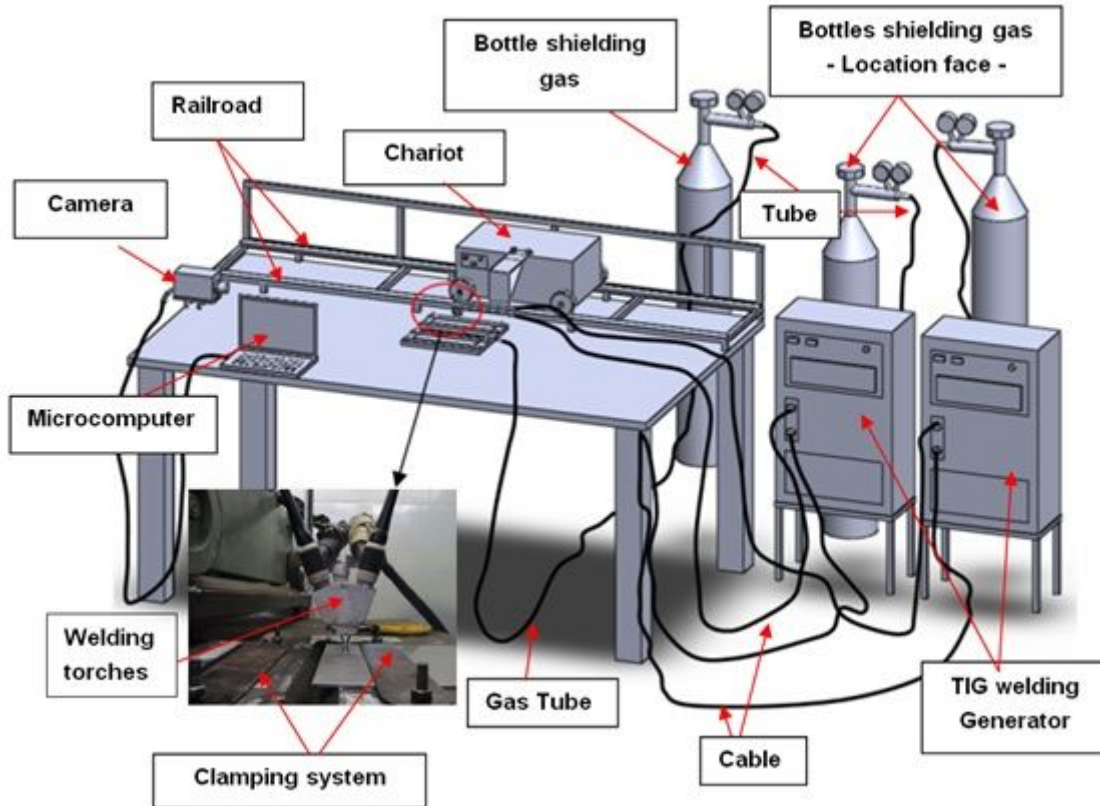


Figure 1

Experimental equipments

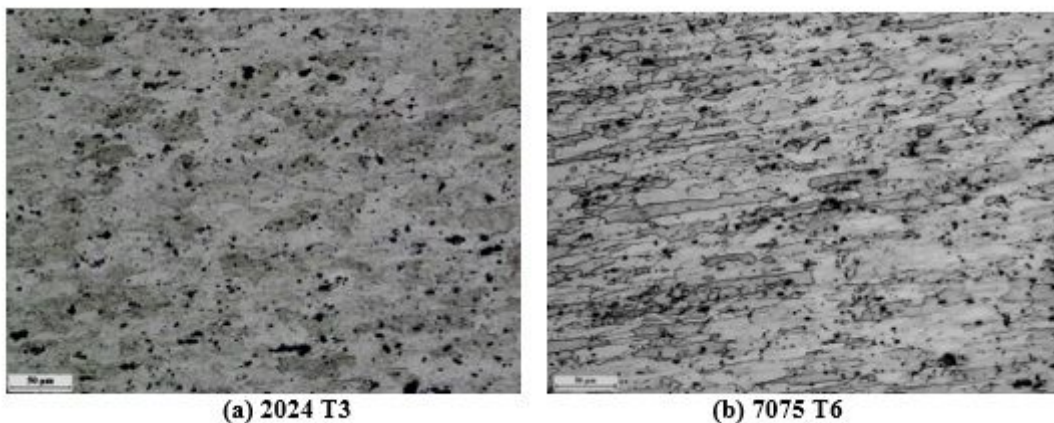


Figure 2

Microstructures of Base Metals

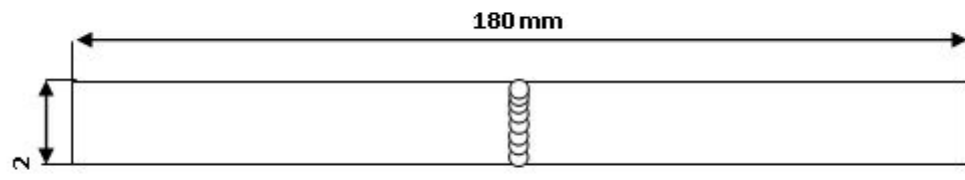


Figure 3

Tensile test piece.



Figure 4

Double Electrode Arc



Figure 5

Welding bead aspects

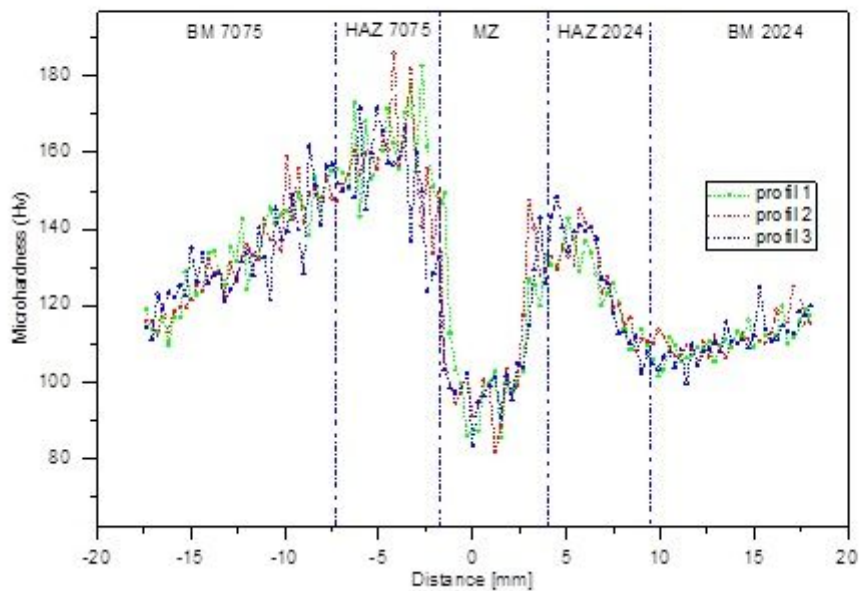


Figure 6

Microhardness profiles across the weldment.

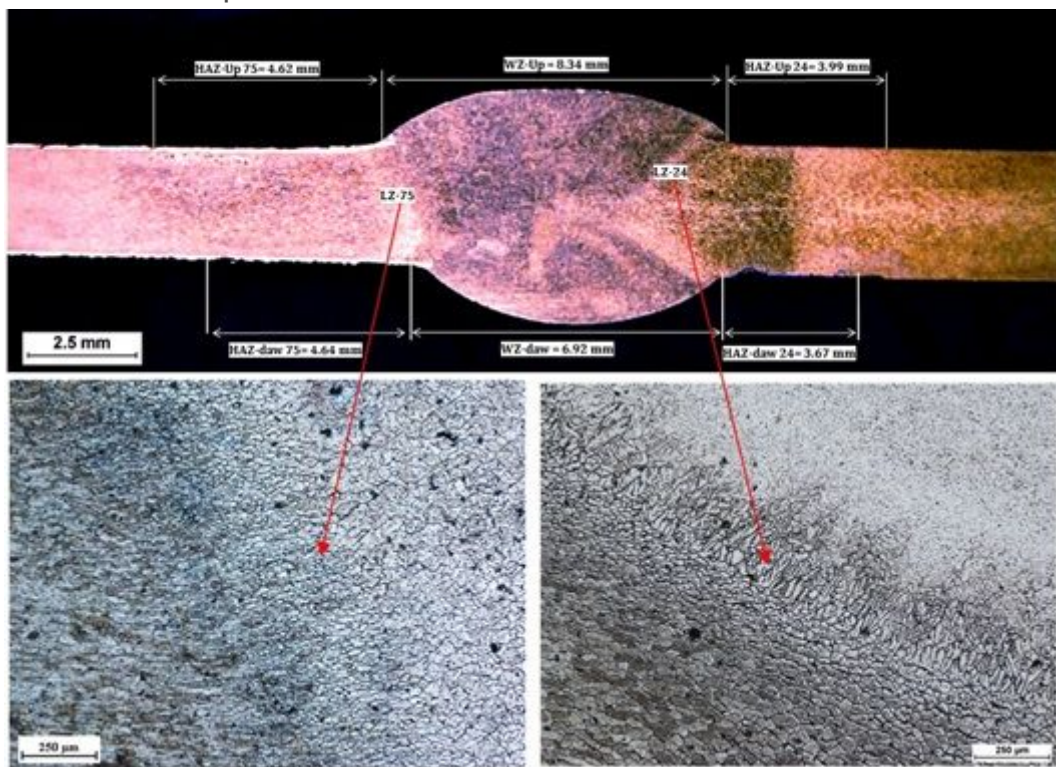
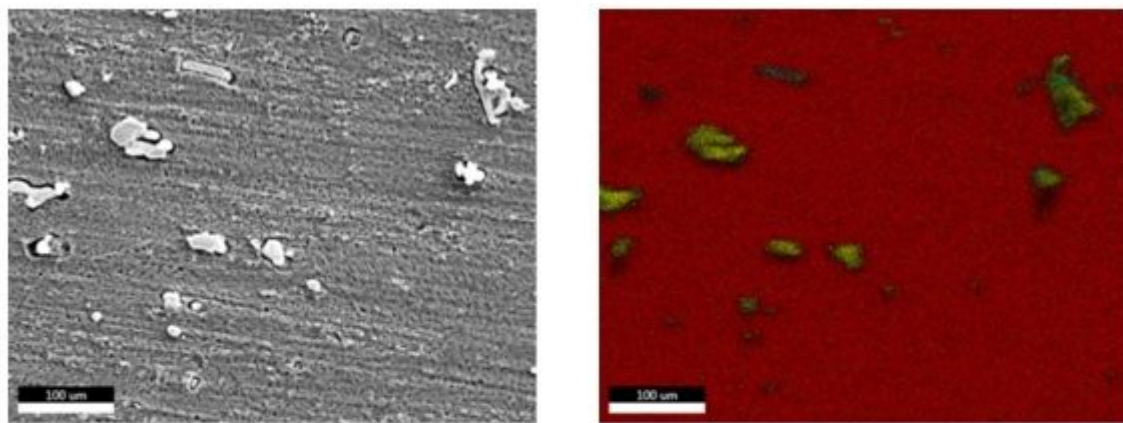
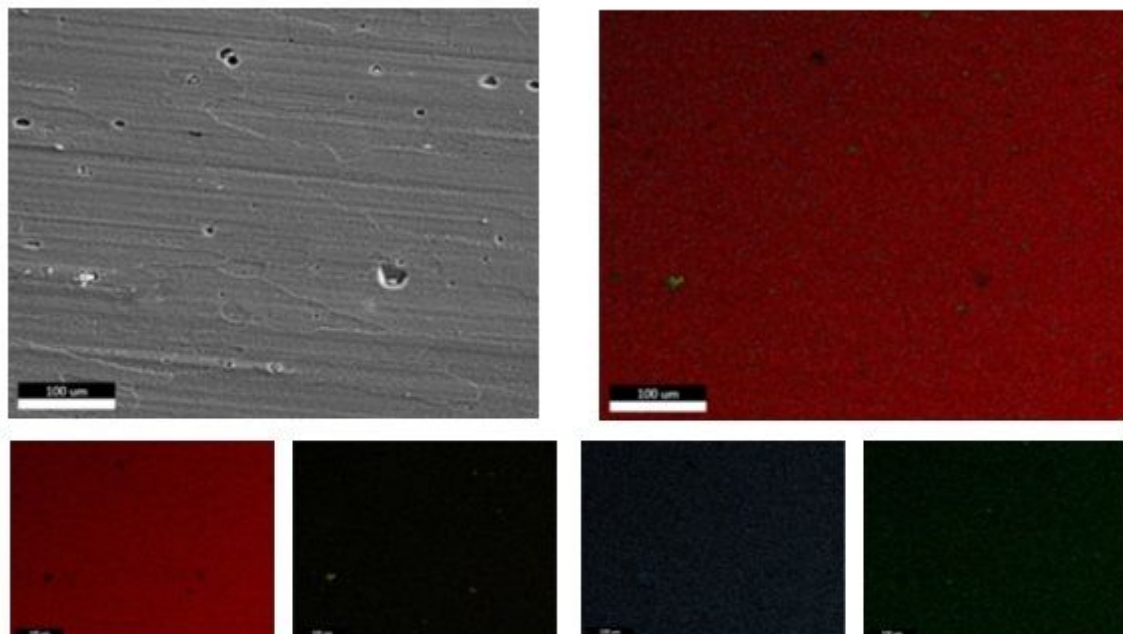


Figure 7

Optical macrograph of the different areas of the welded joint



(a) 2024



(b) 7075

Figure 8

SEM micrograph and EDS chemical analysis of bases metals.

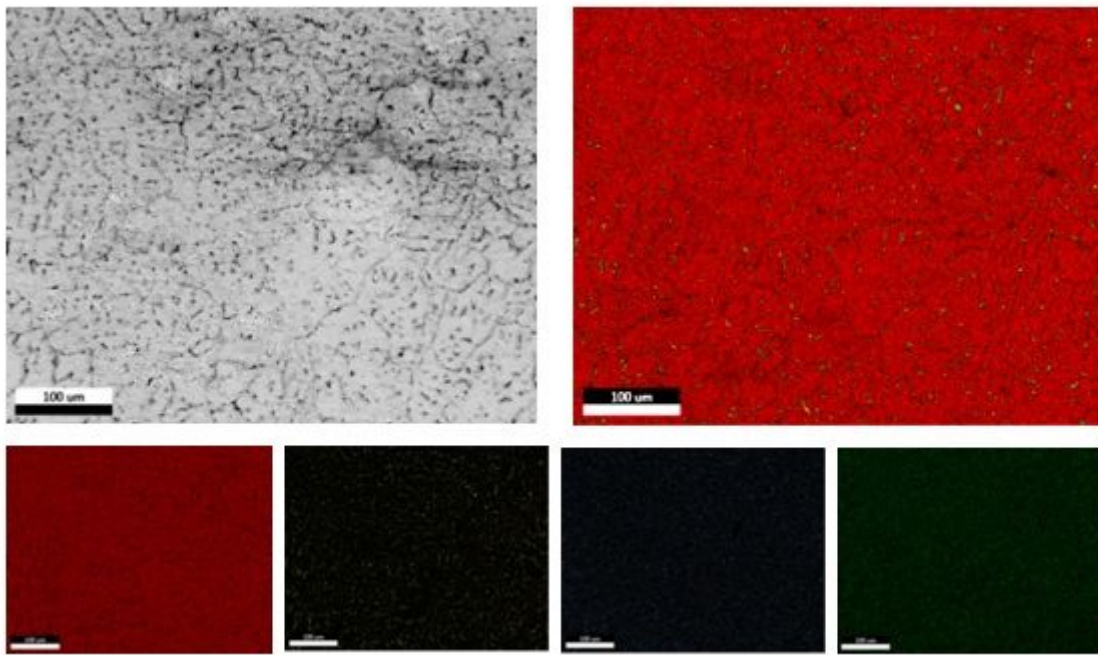
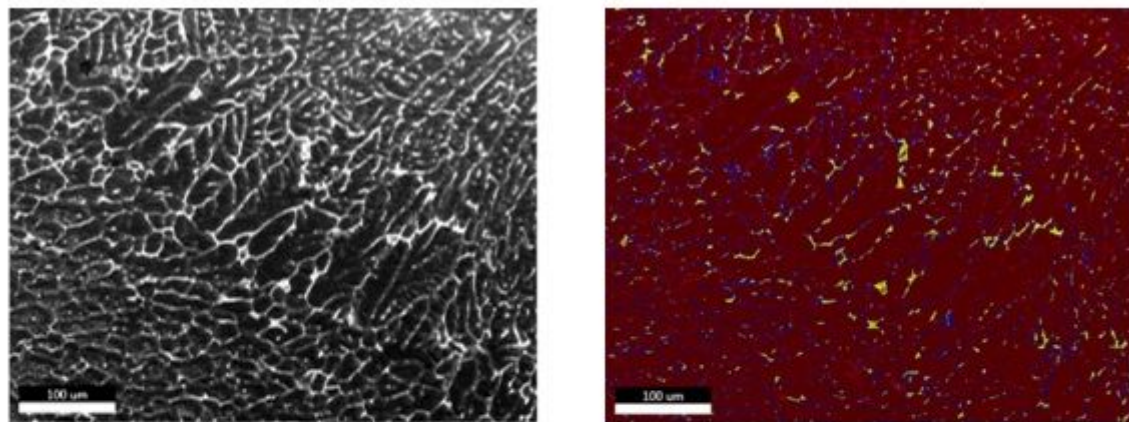
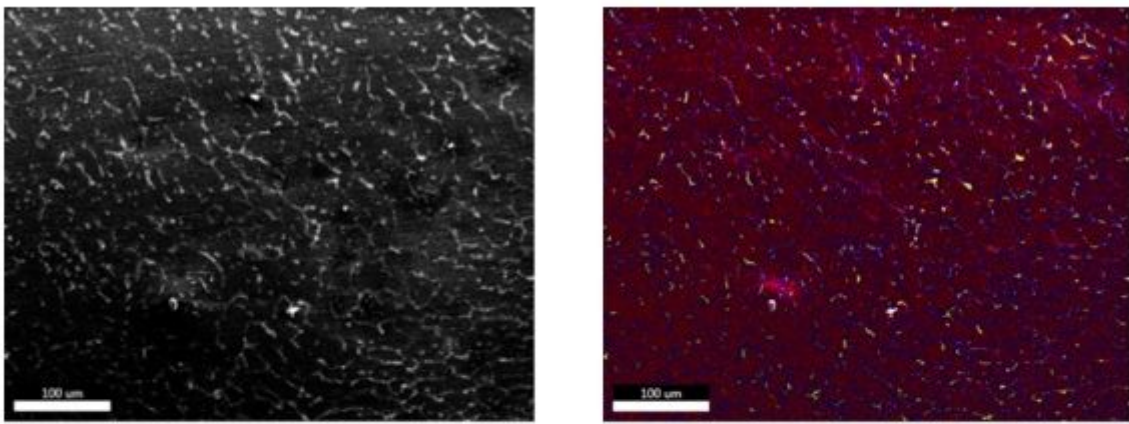


Figure 9

SEM micrographics and EDS chemical mapping analysis of molten zone.



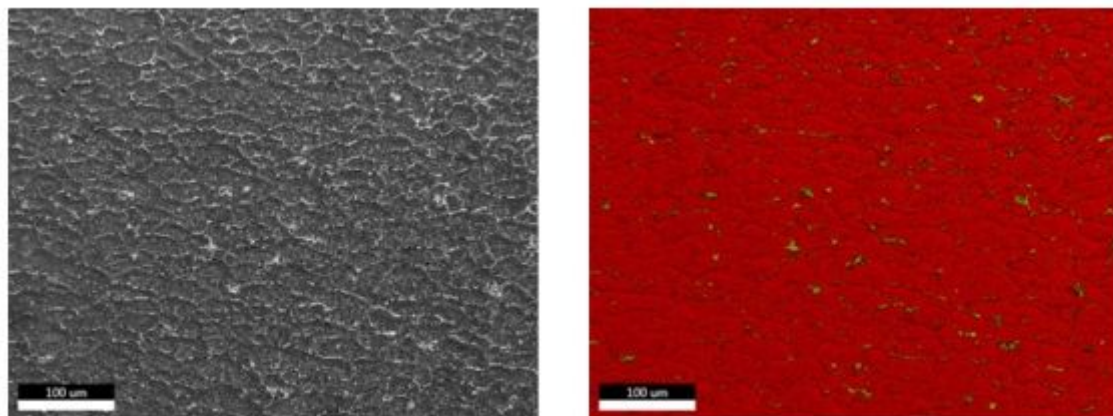
(a) LZ 2024



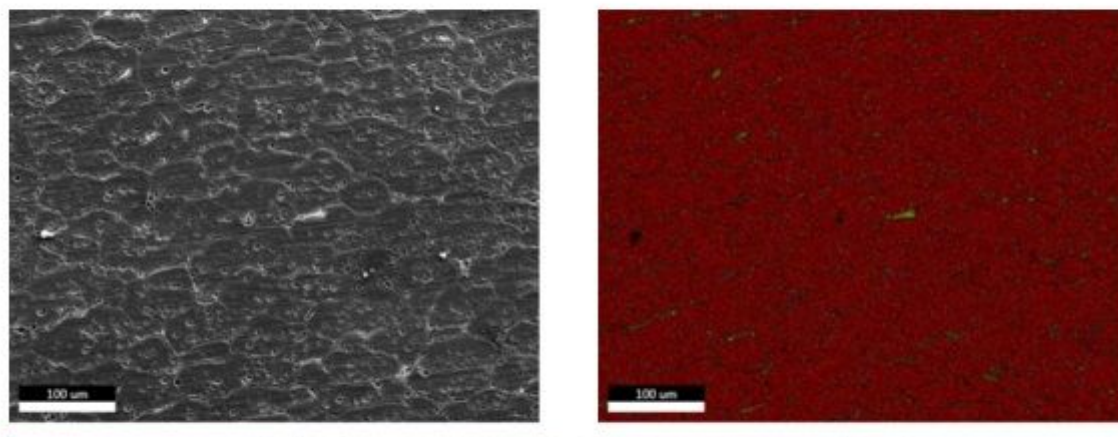
(b) LZ 7075

Figure 10

SEM micrograph and EDS chemical mapping analysis of Liaisons Zones (LZ)



(a) HAZ 2024



(b) HAZ 7075

Figure 11

SEM micrograph and EDS chemical mapping analysis of heat-affected zones (HAZ)

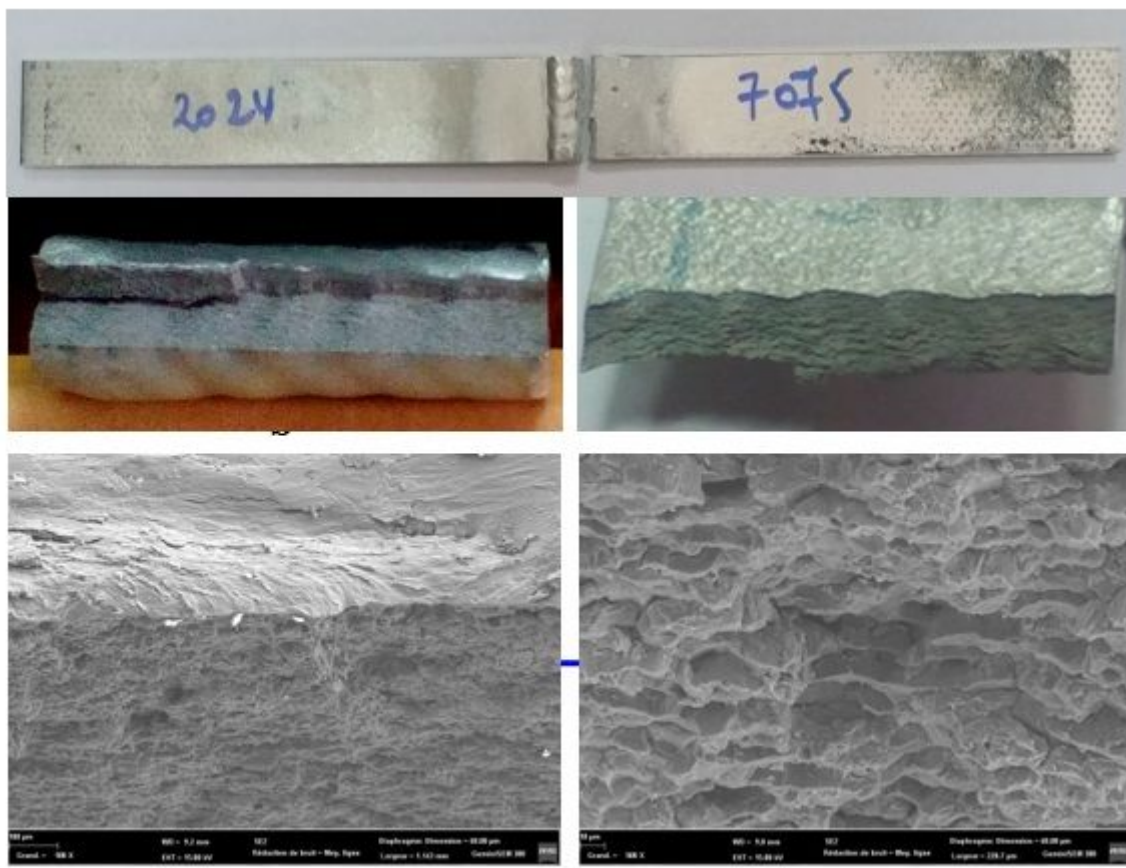


Figure 12

SEM micrograph of the impact fractured in the Weld metal.